Error budgeting and tolerancing of starshades for exoplanet detection

Stuart B. Shaklan,[1a] M. Charley Noecker,[b] Tiffany Glassman,[c] Amy S. Lo,[c] Philip J. Dumont,[a]
N. Jeremy Kasdin,[d] Eric J. Cady,[d] Robert Vanderbei,[d] Peter R. Lawson[a]
[a]Jet Propulsion Laboratory, California Institute of Technology, Pasadena, CA, 91109 USA
[b]Ball Aerospace & Technologies Corp., Boulder, CO 80301 USA
[c]Northrop Grumman Aerospace Systems, Redondo Beach, CA 90278 USA
[d]Princeton University, Princeton, NJ, 08544 USA

ABSTRACT

A flower-like starshade positioned between a star and a space telescope is an attractive option for blocking the starlight to reveal the faint reflected light of an orbiting Earth-like planet. Planet light passes around the petals and directly enters the telescope where it is seen along with a background of scattered light due to starshade imperfections. We list the major perturbations that are expected to impact the performance of a starshade system and show that independent models at NGAS and JPL yield nearly identical optical sensitivities. We give the major sensitivities in the image plane for a design consisting of a 34-m diameter starshade, and a 2-m diameter telescope separated by 39,000 km, operating between 0.25 and 0.55 um. These sensitivities include individual petal and global shape terms evaluated at the inner working angle. Following a discussion of the combination of individual perturbation terms, we then present an error budget that is consistent with detection of an Earth-like planet 26 magnitudes fainter than its host star.

Keywords: Exoplanets, starshades, error budgets, tolerancing

1. INTRODUCTION

With the discovery of hundreds of extrasolar planets in the past 15 years, much attention has been directed to the development of technologies for direct detection and characterization of exoplanets, the ultimate goal being characterization of terrestrial exoplanets orbiting in the habitable zones of their host stars. Coronagraphs, interferometers, and starshades all appear to be viable approaches,[1] but there remain important technical, scientific, and cost tradeoffs between all three.

One of the reasons that starshades have captured the attention of numerous researchers is the realization that allowable perturbations are measured in microns, millimeters, and meters — units that mechanical and thermal engineers are comfortable with, even for large structures. This is in contrast to coronagraphs that must establish and maintain picometer-level wavefronts,[2] or interferometers that require nanometer path length control.[3] Members of the groups that have focused on starshade performance at Northrop Grumman Aerospace Systems (NGAS), Ball Aerospace, Princeton University, and the Jet Propulsion Laboratory (JPL) have collaborated to produce this paper to establish a standardized framework for starshade tolerancing. Our goals have been to 1) identify the main perturbations to be analyzed; 2) develop accurate yet tractable optical models; 3) establish performance goals and an approach to evaluating performance; and 4) present a representative error budget for a strawman mission.

Several authors have reported on starshade perturbation requirements. Mainly they have determined perturbation sensitivities by studying the change in depth of the shadow at the telescope entrance aperture.[4,5,6] While this is a good indicator of which perturbations are the most important to model, pupil-plane studies do not show how and where the scattered light is distributed in the image plane and they are not readily useful for tolerancing and error budgeting. Lyon *et* al,[7] studied sensitivities in the image plane, including single-petal and global-petal truncation terms and alignment sensing and control requirements. Dumont *et al,*[8] in a precursor to the present work, studied image-plane sensitivities and generated a partial error budget consisting of petal truncation, out-of-plane bends, in-plane bends and displacements,

[1]Email: Stuart.B.Shaklan@jpl.nasa.gov; Phone: 818-354-0105

petal edge ripples, and starshade alignment, but did not address global errors. Glassman *et al,*[9] (this conference) have analyzed image-plane sensitivities to the major perturbations described in this paper for a hypergaussian starshade.

In Section 2, we demonstrate that the NGAS and JPL models give consistent perturbation sensitivities. This demonstration is important because these models are the foundation for our tolerancing studies. In Section 3, we describe the main single-petal and global-shape perturbations. Our test case, an optimized design similar to the proposed THEIA mission,[10] is described in Section 4. We then give perturbation sensitivities in Section 5 and use these sensitivities aided with engineering judgment and structural and thermal models to derive an error budget in Section 6. The future direction of our collaborative work is described in the concluding Section 7. The Appendix provides a derivation of the error budget variance and background combination equation.

2. DIFFRACTION MODEL VALIDATION

A key goal of our work has been to develop accurate and tractable optical models. We show that two independent models developed at NGAS and JPL give highly consistent results for both the nominal starshade and perturbation fields.

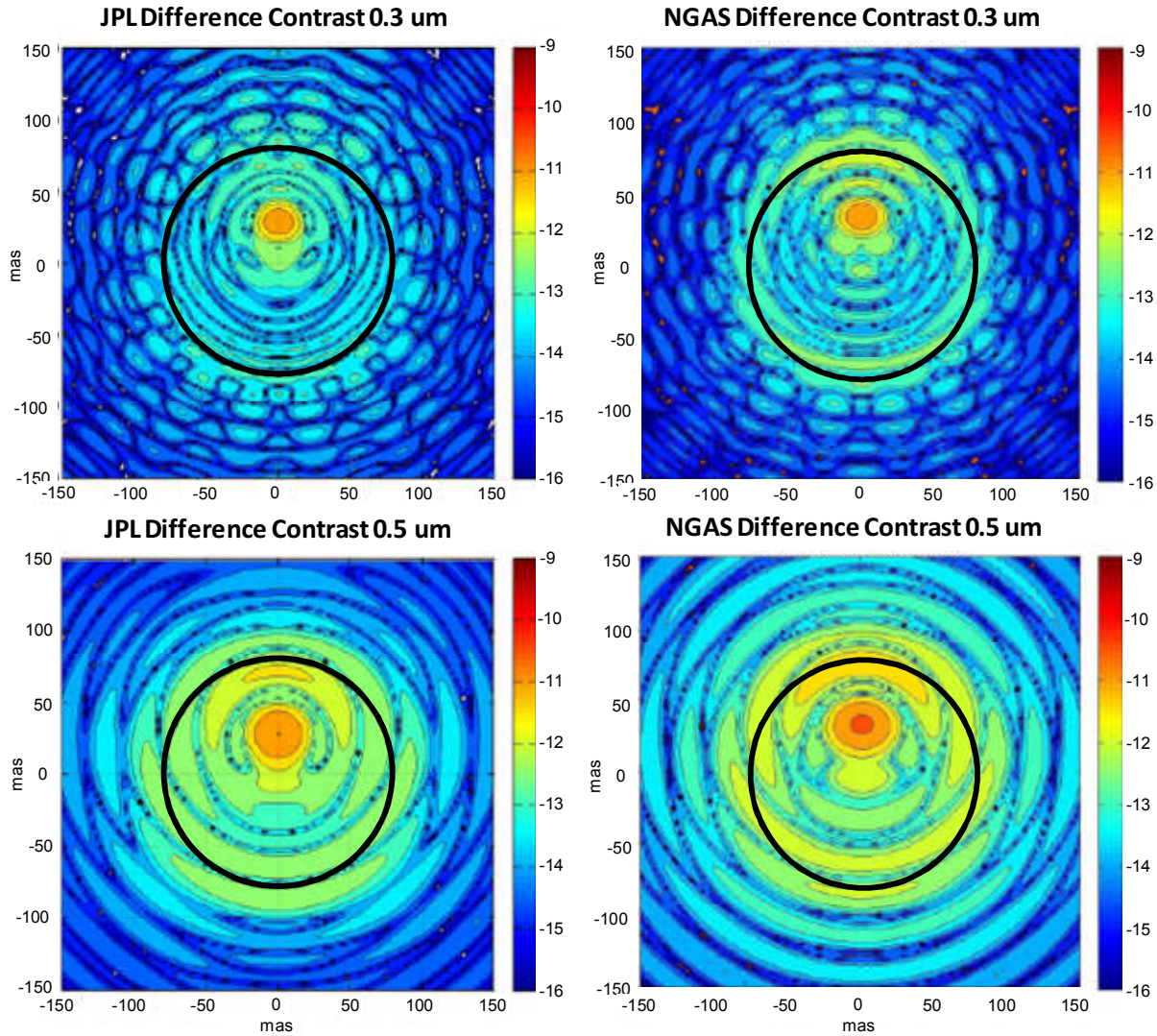

Figure 1. Telescope image plane comparison of the change in contrast for a proportional width perturbation of one part in 10^4. The circle indicates 78 mas, the inner working angle for the tested hypergaussian starshade. Top: wavelength of 0.3 um. Bottom: wavelength of 0.5 um.

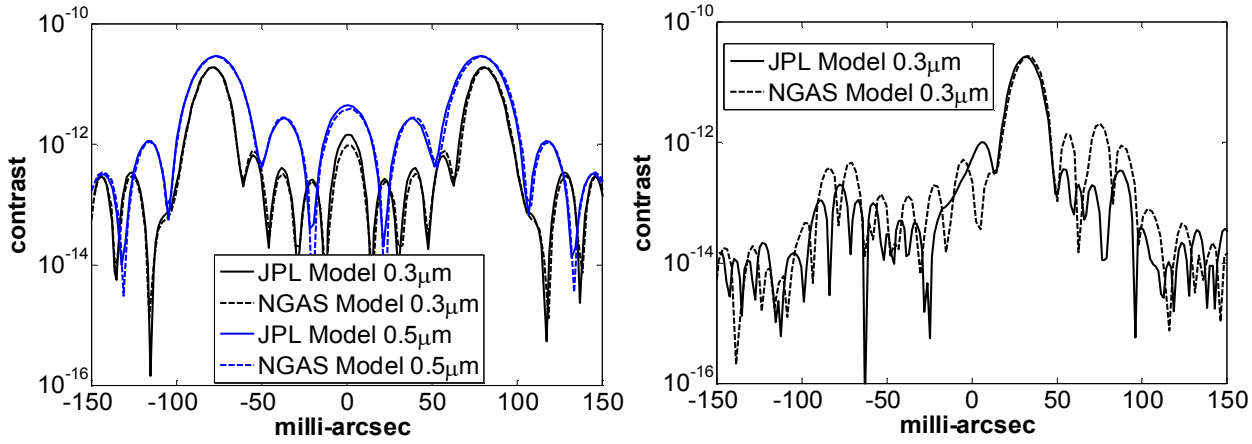

Figure 2: Left: image plane contrast for nominal occulter at λ=0.3 and 0.5 um. The NGAS and JPL (Vanderbei algorithm[11]) codes are in excellent agreement. Right: change in contrast for a proportional width error of 1x10^{-4}, as in figure 1. The codes are in excellent agreement at the peak contrast ~2.5 x 10^{-11}, but the details differ in the side lobes.

The JPL model[8] calculates the electric field at the telescope entrance aperture in two parts. First, the field for the nominal starshade design is determined using the analytic method of Vanderbei et al.[11] This solution is valid for any arbitrary distance behind the starshade that satisfies the paraxial near-field diffraction criterion. Second, the perturbations around the edges of the starshade petals and along the small inter-petal gaps are approximated as an ensemble of small slits. The width of each slit is given by the local width of the defect. The height is determined by dividing the petal length by the number of slits. Based on extensive simulations, we determined that the solution is accurately determined using 512 slits along the edge of the petal. Babinet's Principle is invoked to combine the fields of the nominal starshade and the slits: where petal edges are perturbed to block light that the nominal design passes, the field has negative amplitude. Likewise, where the petals are perturbed to pass light that is nominally blocked, the field has positive amplitude. The fields of the nominal starshade and slits are combined at the telescope entrance aperture and then propagated to the telescope image plane, again using standard techniques.

The NGAS numerical approach is described in Glassman (2010).[12]

Here we show that the NGAS and JPL models yield nearly identical results for a perturbed starshade. We chose a Hypergaussian design[13] with a single perturbed petal and evaluated the image plane contrast at several wavelengths. The 4 m telescope was circular with an unobstructed aperture located on the star-starshade line of sight. The pupil plane sampling resolution was 2 cm and the image plane sampling was 2.52 milli-arcsec/pixel. Image plane intensity was calculated over the bandpass 0.3-1.0 um in steps of 0.1 um. Table 1 lists the parameters of the model using the same notation defined by Arenberg *et al.*[4]

Table 1. Hypergaussian Starshade Parameters

Parameter	Symbol	Value
Solid disk radius	a	12.5 m
Gaussian radius parameter	b	12.5 m
Petal shape parameter	n	6
Occulter separation	F	80,000 km
Number of petals	P	16
Tip cutoff point	r_{tip}	30.6 m

The perturbation was assumed to be a proportional width error symmetric about the petal base-to-tip center line such that the petal width w at a radius r was given by $w(r) = 0.9999 w_o(r)$ where $w_o(r)$ is the nominal design width. For 16 petals around a radius a=12.5 m inner disk, the petal base width is ~4.9 m and the width error was 490 um.

Figure 1 compares the change in image plane intensity computed using the NGAS and JPL algorithms at two wavelengths. Figure 2 shows cuts through the nominal and perturbed intensities. The results agree to better than 5% at the peak of the perturbation but differ substantially in the details of the sidelobes which are an order of magnitude lower.

This does not have a significant impact on sensitivity studies. We have compared these results to a third approach implemented at JPL and based on the algorithm of Dubra and Ferrari.[14] This approach has also been used at the University of Colorado.[6,15] Further, we have verified the JPL codes against the analytical scalar diffraction solution for a uniform circular disk with roughly the same diameter and distance as the starshade in this example. We find excellent agreement with our results and conclude that our models are accurately predicting the nominal and perturbation intensities to better than 5% throughout the nominal field and in the main lobe of the perturbation.

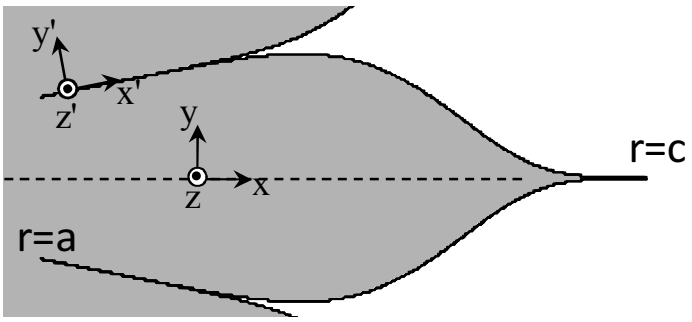

Figure 3. Definition of coordinate axes.

3. STARSHADE PERTURBATIONS

In this section we detail the major starshade perturbations that we expect to most severely impact performance; that is, to produce the largest degradations in contrast. Our goals are twofold:

- To address all of the likely perturbations as completely as possible
- To model the possible deformations and errors as accurately possible with the fewest possible modes and the minimum number of parameters.

Any localized perturbation to the ideal starshade will scatter light that is centered on or near the perturbation and blurred by the resolution of the telescope point spread function. The telescope resolution limit is comparable to or larger than the size of a petal (depending on distance, telescope diameter, and wavelength). Thus, petal perturbations appear as unresolved point spread functions localized at radii at or within the tip of the petal. The scatter is very difficult to distinguish from planet images because it is unresolved and its localized nature leads to little if any lateral spectral smearing.

Perturbations arise through petal manufacture (petal shape and installation into the starshade structure), deployment (petals go to the wrong position and can twist), thermal soak and gradients (petals bend and are displaced), and high-frequency dynamics (reaction wheels cause the petals to move). All of these have both individual petal and global (common to all petals) components that must be modeled.

Global perturbations, e.g., consistent deployment to a too an incorrect position, or systematic manufacturing errors common to all petals, scatter light in a circular pattern that can cause a bright spot to appear in the middle of the starshade image as well as a lumpy ring structure near the petal tips. The scatter forms a localized background field that leads to intensity cross terms that mix with the individual petal perturbations (static, thermal, and dynamic) to effectively add a homodyne 'boost' to the perturbation scatter one would see from the individual petals. A similar effect was seen in the Terrestrial Planet Finder Coronagraph error budget[2] and will be addressed in the Section 4.

Building upon the work of Noecker,[16] we find that the following list of perturbations that follows is sufficiently complete, *i.e.* no major effects are omitted that would likely have a strong effect on final performance of a starshade. Unless otherwise noted, each perturbation has both an individual and global component, and the size of each must be appropriately allocated in a budget for manufacture, deployment, thermal, and dynamic contributions. Figure 3 shows the coordinate system used in our discussion of petal perturbations. We use a localized coordinate system for each petal with the *x*-axis running along the centerline of the petal and the origin at the center of the starshade. The innermost point on the petal, where it meets the disk, is at radius $r=a$. The designed tip location is at radius $r=c$.

3.1 Rigid body position

The petal can be displaced or rotated with six degrees of freedom. Motion along the x-axis (petal moves radially toward or away from the disk) is an example of a perturbation that adds or removes energy from the shadow; the top and bottom petal edges block or pass light relative to the nominal design. When this error appears globally on all petals, it increases the bias level of the shadow and therefore increases the homodyne boost. This is illustrated in the second and third rows of Figure 4. The starshade/telescope combination used for Figure 4 is described in Section 4.

Motion along the y-axis has a differential effect on the shadow: the petal moves to block light on one edge that would be transmitted in the nominal design, while passing light on the other edge that is blocked in the nominal design. This produces a dual-lobed pattern whose single-petal leakage may be as large as an additive perturbation but has almost no effect as a global error (common to all petals). This is seen in the 5th row of Figure 4, which is nearly identical to the top row (nominal contrast).

Motion along *z* has no effect unless the starshade has been tilted by a large angle relative to the star-telescope line of sight. This large tilt is sometimes needed to keep sunlight off the visible side of the starshade. The tilt couples out-of-plane motion to apparent in-plane motion and changes the projected shape of the starshade. Rotation about the *x*-axis causes a proportional width error. This adds field to the shadow.

Rotation about the *z*-axis is an in-plane rotation with a differential field effect. We assume the petal rotates about the axis $x=a$ at the base of the petal.

Rotation about the *y*-axis, again at $x=a$, foreshortens the petal (unless the starshade is tilted, where it can appear to stretch the petal). Because the petal is wider at its midpoint than at its base and tip, *y*-rotation can simultaneously block more light (relative to nominal) along part of the petal while passing more light along others.

3.2 Shape errors

Ripples

Petal shape perturbations can be expressed in terms of a Fourier series along each edge, e.g. the in-plane edge azimuthal error is given by $e(r) = \sum_N a_N \sin N\pi(r-a)/(c-a)$, where a and c are the petal base and tip positions, and N is an integer. Symmetric errors, where the petal edges move inward or outward at each radius, thus leaving the centerline unchanged, are more important than asymmetric errors that shift the centerline without changing the petal width. The largest scattering occurs when the sinusoidal period is roughly equal to twice the Fresnel zone spacing. The Fresnel number is given by $F = r^2/\lambda L$, where r is the radius, λ is wavelength, and L is distance to the starshade. For the starshade design and bandpass discussed in Section 4, the Fresnel number change from the inner petal edge to the tip is ~ 8 at the long end of the bandpass, and ~16 at the short end. Thus we expect to see the peak sine wave sensitivity occur between 4 and 8 cycles/petal for this design.

Ripples can occur out of plane as well but these only have an effect when the starshade is tilted. Their contribution to scatter will be significantly less than the in plane effects as long as the perturbation amplitudes are comparable.

Petal Bends

Lateral (in plane) petal bending occurs when both edges of a petal are displaced tangentially in the same direction (along *y*) with each point on the edge moving according to a collection of functions with $(r-a)^n$ dependence. The actual structural modes can be expressed as linear combinations of these functions. In our models the length of the petal is preserved so that the tip moves in radially as well as azimuthally.

Note that $n=0$ is equivalent to a rigid body translation of the petal and $n=1$ is equivalent to a rigid body rotation about the *z*-axis through the base of the petal. We have modeled translation, rotation, and quadratic bends ($n=2$).

Out of plane bends (motion along *z*) are similarly expressed by polynomials in $(r-a)^n$. Quadratic out of plane bends correspond to uniform bending on a constant radius leading to a foreshortening radially-in-plane. This is accounted for in our models.

Petal Size and Length

The petals are typically several meters wide at their base, growing radially for a few meters until the apodization function takes over and tapers them to a pointy tip. There are two kinds of shape errors likely to occur in manufacturing; constant, and proportional width and length errors. Since the tips are long and narrow, the metrology of the tip shape

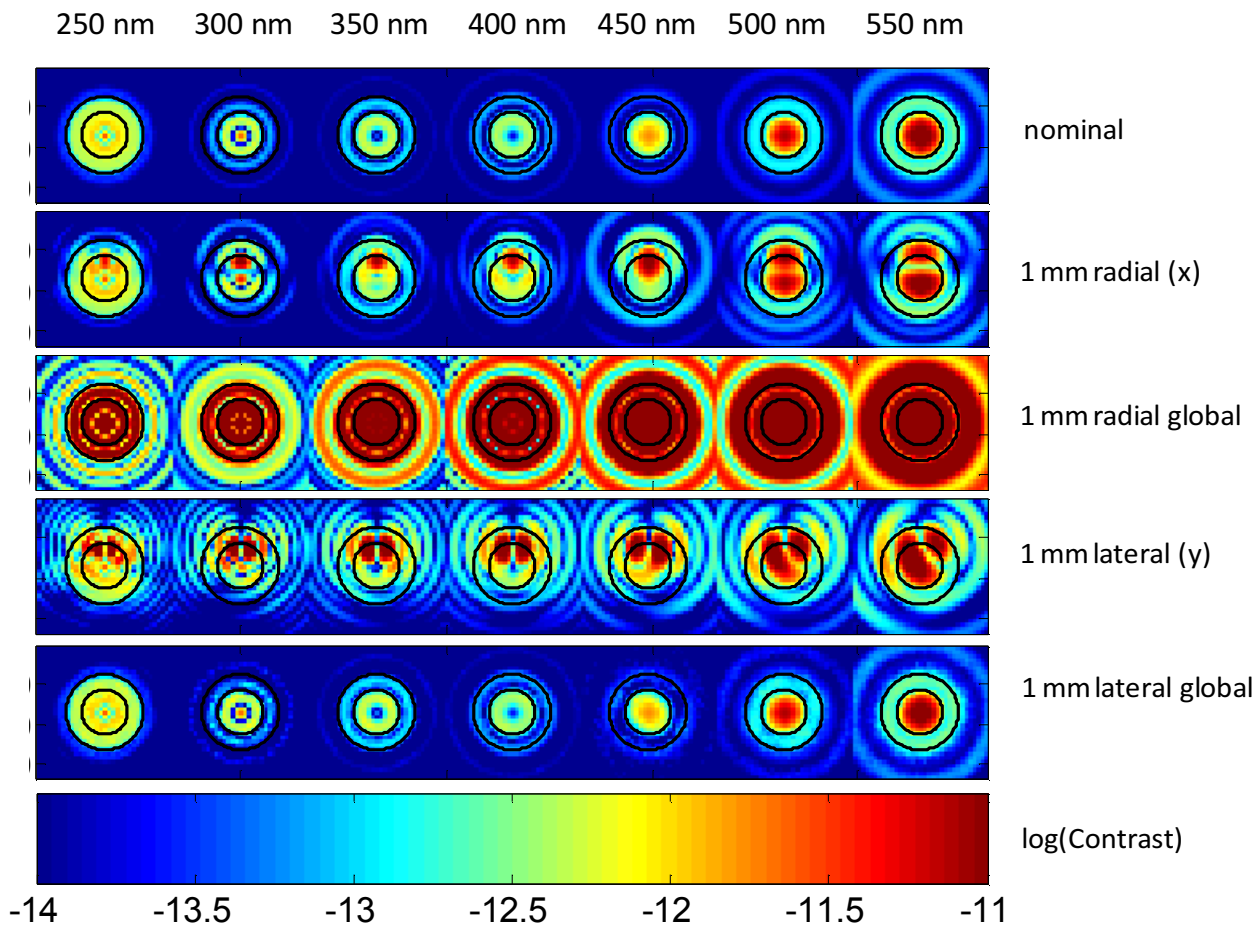

Figure 4. Image plane contrast vs. wavelength for the nominal design (top), a 1 mm radial perturbation on one petal (2nd row), and then applied to all petals (3rd row), a 1 mm lateral perturbation on a single petal (4th row), and the same 1 mm lateral perturbation on all petals (5th row). Circles indicate swath used for measuring contrast, centered at 90 mas, with a width of 46 mas. The starshade and telescope are the 34-m / 2-m design described in Sect. 4.

will almost certainly be more accurate than the wide parts of the petal. A full-fledged error budget should carry fixed width errors separately for the petal and tip. In this work, we have modeled a proportional width error of 10^{-4}, with a minimum width error of 25 um anywhere along the petal.

Tips that are truncated due to manufacture or deployment error will scatter light. Tip truncation is included in our modeling. Likewise, the location of the petal base, *i.e,* the outer edge of the central disk, affects the apodization profile. We have not modeled this term but it is expected to be less important than the tips since it is at the base of the petal (far from the planet) and there are drivers (e.g. radial petal position) that will demand the central disk inner edge perturbation be substantially less than the petal tip truncation.

An implication of petal width errors and petal displacements is that in some designs the narrow valleys between the petals can be blocked. In the design discussed below, the minimum valley width is 1 mm and the proposed implementation based on a perimeter truss does not allow petal displacements of this magnitude. However, in some designs the gaps are substantially smaller and this effect should be modeled as well.

3.3 Holes

Holes in the starshade allow starlight to transmit directly to the telescope. The scattered field from one hole through a single layer is

$$\delta E_1 = E_0 \frac{\pi a^2}{4\lambda F} \tag{1}$$

where a is the diameter of the hole, λ is the wavelength, F is the distance to the telescope, and E_0 is the field of the incident starlight. A 1 cm diameter hole yields a uniform intensity of 3.2×10^{-12} at the telescope entrance at λ=550 nm and F=80,000 km.

If N holes are sprinkled across the starshade, their field contributions add coherently, yielding a factor as large as N in field and N^2 in intensity. However, the fields of the holes are not all in phase, because of the Fresnel phase:

$$\phi_F = \frac{\pi r^2}{\lambda F} \tag{2}$$

where r is the hole's distance from an axis from the star through the starshade to the telescope. If all N holes were confined within about 2m around the axis, they would give nearly the maximum intensity factor N^2. If spread over the entire starshade, the sum of holes quickly cancels, falling as $\text{sinc}^2(\phi_F/2)$. But this cancellation is limited by the telescope pixel's footprint at the starshade. Minimum suppression occurs for on-axis pixels (those aimed at ρ=0); but suppression is quite strong for pixels aimed at other parts of the starshade, which span several Fresnel zones. For an on-axis pixel, the net (coherent) flux is roughly

$$\delta I_N = I_0 \cdot \left(\frac{A_h}{\lambda F}\right)^2 \cdot \text{sinc}^2\left(\frac{2A_p}{\lambda F}\right) \tag{3}$$

where A_p is the area of the pixel's footprint on the starshade, and $A_h = N\pi a^2/4$, the total area of all holes. For a 2m telescope, critically sampling pixels, λ=550 nm, and F=39,000 km (see test case below), minimum suppression is roughly a factor 6, and the intensity is 10^{-12} for holes totaling 1 cm^2 over a 23 m^2 region in the center of the starshade (2.3×10^{-6} coverage).

This analysis assumes each pinhole is like an ideal aperture in a single-layer thin screen. But all designs considered so far have used multiple layers of "plastic" sheet with mm-scale spacing. If a micrometeoroid were to puncture all layers, the result is a series of pinholes illuminated by other pinholes. Even if all the holes were aligned toward the telescope, this reduces the transmitted field strength at each layer, and also scrambles the phase of the final transmitted field. This will cancel the leakage fields at the telescope even more effectively. Thus the tolerances outlined above are conservative, and can probably be relaxed after further analysis.

Preliminary engineering studies accounting for micrometeorite flux show that for multi-layer designs, maintaining the transmissive hole area to < 1 cm^2 is feasible.[17]

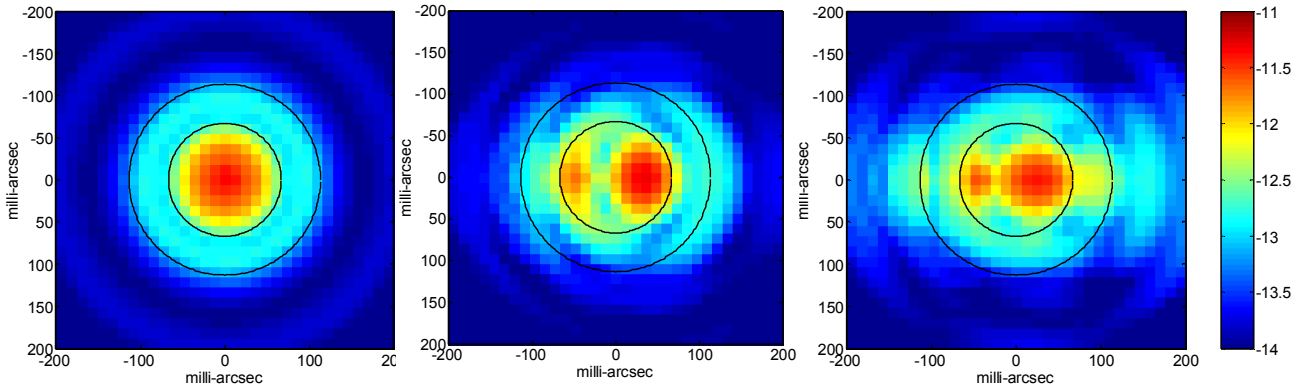

Figure 5. Log of the contrast for the ideal starshade: a) on axis, b) with 1 m cross-track motion; and c) with 1.4 m cross-track motion. The images are a composite of the uniformly weighted bandpass 0.25 – 0.55 um. The starshade is described in Sect. 4.

3.4 Starshade positioning

A final source of coherent scatter is the motion of the telescope in the shadow of the starshade. The shadow is designed to extend several meters off-axis. When the telescope drifts through the shadow, the electric field changes slightly and this mixes with leakage from other perturbations. Like global perturbations, this boosts the sensitivity to individual petal perturbations.

While the effect on electric field is linear with perturbation amplitude for petal and global terms, making it straightforward to perform Monte-Carlo simulations in the image plane of the telescope, this is not the case for starshade positioning errors. To add positioning errors requires computing the nominal shadow at the telescope pupil plane, then computing the Fourier Transform of the field at the image plane. Figure 3 shows examples of the scattered intensity at several offset positions. In Section 5 we show how a 1-m offset affects the error budgeting.

3.5 Edge sharpness

Sunlight is incident on the edge of the starshade and some of this light scatters toward the telescope. This scatter is a function of the length and shape of the petal edge, its reflectivity and scatter characteristics, and the radius of curvature (RoC) of the edge. It is negligible for razor-sharp edges and appears to become significant when the RoC approaches 25-100 um.[17]

Scatter from edges adds a localized but incoherent background to the observed light. The scatter is simply additive and must be controlled by the sharpness of the edge and material properties. This concern is mitigated by constraining the starshade alignment so that sunlight is always incident on the back (star) side of the starshade with at least a few degrees of margin. The edge sharpness and reflectivity requirements will be addressed in a future paper.

4. TEST CASE

A wide range of starshade missions have been proposed in the literature, with starshade tip-to-tip diameters ranging from 14 m with a 1.1-m telescope,[18] to 70 m class starshades for JWST.[19] For this paper, we have chosen an intermediate design similar to THEIA[10] and the Occulting Ozone Observatory,[20] using an optimized occulter[21] design by E. Cady with a 2 m telescope having a 0.4 m central obscuration.

This reference starshade is optimized to work over the bandpass 0.25 – 0.55 um and to provide 10^{-12} suppression at the inner working angle. It has a 34 m diameter tip-to-tip, with 6.5-m long petals and a 21-m diameter central disk. It has 30 petals but could work equally well with 16. With 30 petals, the minimum gap between petals is 1.07 mm, as is the minimum width of the petal tip. These increase to 2 mm for a 16-petal design. The starshade is positioned 39,000 km from the telescope. A similar design is discussed in Thomson and Lisman (this conference).[22]

For our study, we assume the telescope is an ideal diffraction limited instrument. The pixel scale in the image plane is 12 milli-arcsec per pixel, which gives two pixels per FWHM or > 5 pixels across the main Airy lobe at the shortest wavelength.

5. PERTURBATION SENSITIVITIES

We have studied 16 independent perturbations applied to single petals and globally to all petals. For single petal perturbations, we found the perturbation amplitude that results in a peak contrast of 10^{-12} in any wavelength band spanning 0.25–0.55 um, within an annular region centered at the inner working angle. The annulus had a width equal to the full-width at half max (FWHM) for the telescope point spread function evaluated at a wavelength of 0.45 um (see Figures 4 and 5). We studied two inner working angles: 90 mas, corresponding to the apparent angle of the petal tip seen by the telescope, and 75 mas, about 3 m in from the tip where the throughput is ~ 54%. The bandpass was modeled at seven discrete wavelengths; 0.25, 0.30, 0.35, 0.40, 0.45, 0.50, and, 0.55 um.

Table 2 lists the perturbations of a single petal, the amplitude for which the peak contrast reaches 10^{-12}, and the wavelength where the peak sensitivity occurs. The amplitudes are listed for both 90 and 75-mas working angles. For the ripples, the amplitudes given are the peak sine-wave amplitude; the r.m.s. value is 0.71 times the listed amplitude. In many cases, the values for 90 and 75 mas are the same because the inner edge of the 90 mas IWA annulus captured the

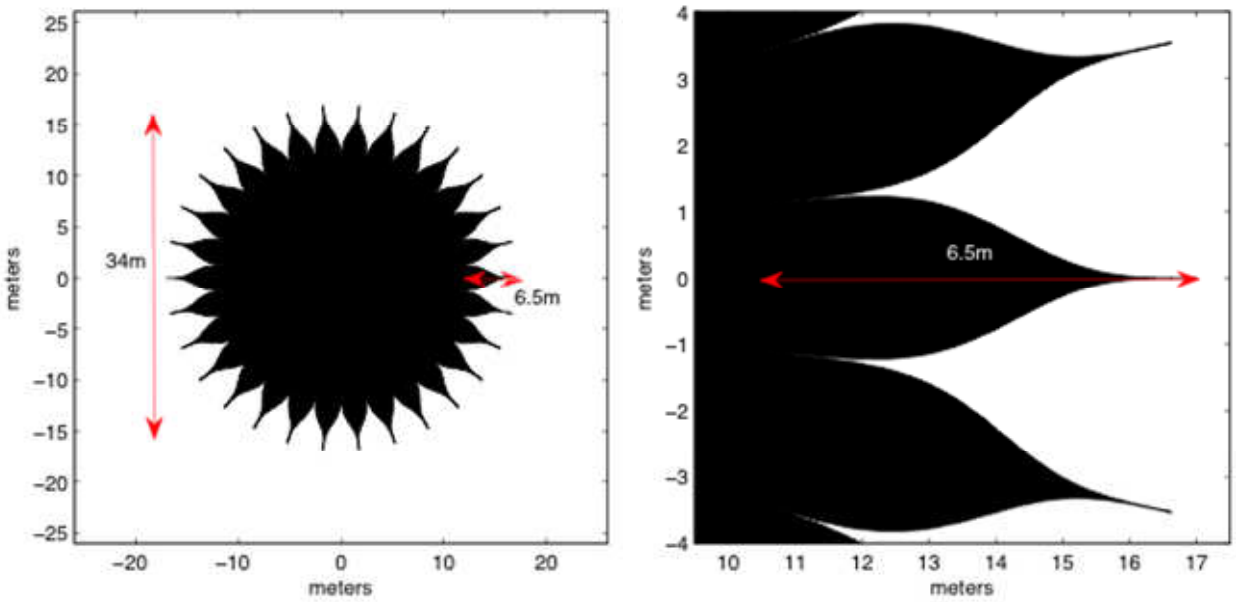

Figure 6. Occulter design for our study. Located ~ 39,000 km from the telescope, the Fresnel number is 29.6 at the shortest wavelength 0.25 um, and 13.5 at the longest wavelength 0.55 um.

peak scatter which may have occurred closer to 75 mas. The starshade was assumed to be viewed face-on, in perfect alignment with the star, and opaque out to the edges (no holes).

Some perturbations have a very weak impact. The petal tips can be 9 mm too long or too short before contrast increases by 10^{-12}. Out-of-plane bending of > 0.5 m is allowed (but this will be tighter when the starshade is tilted). For in-plane rotation about the base of the petal, the tip can move ~ 5 mm. The tip motion for in-plane bends can be up to 32 mm. Ripples at very low frequency (1 cycle/petal) and high frequency (> 16 cycles/petal) can have amplitudes > 50 um. Elliptical distortion of the 21-m perimeter truss, amounting to eccentricity of 0.02 or 1 mm change in semi-major axis, gives peak contrast at 0.55 um of $4 \times 10^{-13}$and a mean background of 4.5×10^{-13}.

The most sensitive perturbations are in the symmetric ripples at periods double the Fresnel zone spacing. For periods from 4 and 8 cycles/petal the sine-wave amplitude should be < 3-4 um.

For global perturbations in which the perturbation is identical on all the petals, the scatter is circularly symmetric with very little ripple. Rather than measure peak contrast, we have determined the perturbation amplitude that raises the mean contrast level in the annulus to 10^{-12} (Table 3). The disparity between additive (e.g. radial shift) and differential (e.g. lateral shift) perturbations, noted in Figure 4, is quantified here. A common radial shift of just 110 um raises the background by 10^{-12}, compared to 350 um for a single petal. The amplitude for the global lateral shift (equivalent to a *z*-rotation of the whole starshade plus a small *x*-translational and *z*-rotational component of the petals) is 19 mm, about 50 times larger than the single petal value. Note that the 19-mm value is the result of scaling a much smaller shift. We did not model the potential petal overlap and disk-petal gaps that would occur with such a large shift.

The scatter is particularly sensitive to global symmetric sine terms on the petals. Sine waves of 4-8 cycles/aperture, with 1-2 um amplitudes, if symmetric about the petal center line (or 2-4 um if on one petal edge) will raise the background level by 10^{-12}. The manufacturing process should avoid ripples in this range that are common to all the petals. It may also prove difficult to verify that the petals have been manufactured to the micron level.

We have also modeled a global shape perturbation, the planar elliptical deformation of the supporting truss in our design.[22] Some amount of eccentricity will arise during deployment. We find that the eccentricity that raises the peak contrast by 10^{-12} in the 90 mas IWA annulus is 0.032, corresponding to a semi-major axis change of ~5 mm over the 21-

m central disk diameter. Likewise, the eccentricity that raises the mean contrast level in the 90 mas IWA annulus by 10^{-12} is 0.03. This planar mode is not one of the low-order structural modes. Non-planar modes are more likely to be excited by dynamic and thermal perturbations and may play an important role if the starshade is not viewed face-on.

Table 2. Single petal contrast sensitivity

		90 mas		75 mas		
No.	Perturbation	Amplitude	Wavelength (um)	Amplitude	Wavelength (um)	Units
1	Proportional width	3.06E-05	0.50	2.90E-05	0.50	n/a
2	Tip clip	9.13	0.25	9.13	0.25	mm
3	Radial shift	0.35	0.55	0.29	0.55	mm
4	Quadratic out-of-plane bend	>500	0.25	>500	0.25	mm
5	lateral shift	0.20	0.30	0.14	0.25	mm
6	In plane rotation	4.97	0.50	4.81	0.35	mm at tip
7	In plane quadratic bend	32.32	0.50	30.50	0.25	mm at tip
8	Symmetric sine wave 1 cycles	89.67	0.50	83.59	0.50	um
9	Symmetric sine wave 2 cycles	36.82	0.50	34.55	0.50	um
10	Symmetric sine wave 4 cycles	4.05	0.55	4.05	0.55	um
11	Symmetric sine wave 8 cycles	3.29	0.30	3.29	0.30	um
12	Symmetric sine wave 12 cycles	9.02	0.25	9.02	0.25	um
13	Symmetric sine wave 16 cycles	30.71	0.25	30.71	0.25	um
14	Symmetric sine wave 20 cycles	59.68	0.25	59.68	0.25	um
15	Antisymmetric sine wave 4 cycles	63.40	0.40	62.00	0.40	um

Table 3. Global contrast sensitivity: all petals contribute equally.

		90 mas		75 mas		
No.	Perturbation	Amplitude	Wavelength (um)	Amplitude	Wavelength (um)	Units
1	Proportional width	1.03E-05	0.50	1.03E-05	0.50	n/a
2	Tip clip	6.67	0.55	6.67	0.55	mm
3	Radial shift	0.11	0.55	0.11	0.55	mm
4	Quadratic out-of-plane bend	> 500	0.35	>500	0.35	mm
5	lateral shift	12.30	0.55	9.60	0.55	mm
6	In plane rotation	157.62	0.55	157.62	0.55	mm at tip
7	In plane quadratic bend	>500	0.55	>500	0.55	mm at tip
8	Symmetric sine wave 1 cycle	31.16	0.50	31.16	0.50	um
9	Symmetric sine wave 2 cycles	12.27	0.50	12.27	0.50	um
10	Symmetric sine wave 4 cycles	1.21	0.55	1.21	0.55	um
11	Symmetric sine wave 8 cycles	2.18	0.30	2.18	0.30	um
12	Symmetric sine wave 12 cycles	6.96	0.25	6.96	0.25	um
13	Symmetric sine wave 16 cycles	24.48	0.25	24.48	0.25	um
14	Symmetric sine wave 20 cycles	38.76	0.25	38.76	0.25	um
15	Antisymmetric sine wave 4 cycles	>500	0.55	>500	0.55	um

6. ERROR BUDGET

6.1 Requirements

The ultimate goals of the exoplanet detection mission are to detect and characterize earth-like planets in the habitable zone of their host stars. Several studies[23,24] have shown that to have a reasonable likelihood of detecting several planets, the mission should be able to detect planets that are 26 magnitudes fainter than their stars, at angular distances < 100 mas. The IWA considered in our study is 90 mas.

We require the signal-to-noise ratio (SNR), defined as the ratio of the peak planet signal to the root-mean-square systematic noise floor on spatial scales similar to the planet PSF, to be SNR > 4. The requirement applies to each wavelength considered, 0.25, 0.3, 0.35,…,0.55 um. Thus, for a planet with Δm=26 (peak planet contrast = $4x10^{-11}$), we require the instrument noise floor to be below $1x10^{-11}$ relative to the peak of the star image in the absence of the starshade. NASA is presently funding studies that will explore the effectiveness of this criterion but for now it seems reasonable to require SNR > 4 at the IWA of 90 mas.

As noted earlier (Figures 3 and 5), we evaluate the performance versus this requirement using an annulus centered on the IWA, with a FWHM equal to the width of the PSF at 0.45 um. This allows us to capture all of the light in the core of a planet image centered at the IWA, while considering the effects of the scatter gradients throughout that zone.

In this work, we consider neither the potential benefits of spinning the starshade nor post-processing to eliminate deterministic systematic errors. Spinning will eliminate the local variability due to fixed errors arising from manufacturing and deployment errors, and to an unknown extent, thermal gradients. Post-processing based on algorithms such as LOCI[25] may provide benefit as well although gains may be limited by the proximity of the IWA to the optical axis. On-sky calibration will eliminate some systematic errors but the effectiveness has not been studied to date.

6.2 Approach

We present a top-level error budget (Table 4) that is a combination of individual petal and global contributions, the modal deformation, and starshade-telescope (cross-track) alignment errors. The cross-track error proved to make very little difference for offsets < 1-m and will not be considered further in this paper. This budget must ultimately be sub-allocated into manufacturing, testing, deployment, thermal, and dynamic budgets. We have not done this because the specific sub-allocations will depend on the starshade mechanical design, e.g. whether petals are folded, the nature of deployment mechanisms, structural damping, etc. The error budget is calculated at seven wavelengths, 0.25, 0.3,…,0.55 um and each band is treated as monochromatic.

We have set up a spreadsheet representation of the error budget and have verified our error term combination approach using Monte-Carlo (M-C) simulations of the perturbed starshade. To set up the spreadsheet, we first calculated the r.m.s. and mean contrast sensitivities for a given amplitude of each of the 31 independent perturbation fields (15 each from tables 2 and 3, plus the elliptical modal shape) without adding in the nominal background. We then used engineering judgment to allocate amplitudes for the perturbations and assumed that for small changes in amplitude the scattered energy scaled as the square of the perturbation amplitude. This behavior was confirmed by our optical models. Allocations were modified so that the error budget requirement of r.m.s. contrast in all bands was better than 10^{-11} in the IWA annulus.

The variance of the scatter is computed using the expression whose derivation we give in the Appendix:

$$\sigma^2 = 2\langle I_b \rangle \langle I_r \rangle + \sigma_r^2 \tag{4}$$

where $\langle I_b \rangle$ is the expectation over the ensemble of possible perturbation values of the sum of the radially-dependent mean intensity background from global terms plus the intensity of the nominal background (from the unperturbed starshade) plus the intensity contribution from holes (these were not included here) and cross-track error. $\langle I_r \rangle$ is the expectation of the sum of the mean intensity background over all the individual petal terms and the modal term, and σ_r^2 is the sum of the variance of the intensity scatter over all the petals and the modal term. These means and variances

Table 4. Error Budget Requirements

No.	Perturbation	Single Petal 1-sigma	Global tolerance	Units	r.m.s. contrast	Global Mean Contrast
1	Proportional width	2.50E-05	2.00E-05	n/a	**2.6E-12**	**1.6E-12**
2	Tip clip	4	4	mm	2.6E-13	3.3E-13
3	Radial shift	0.30	0.20	mm	**3.2E-12**	**1.4E-12**
4	Quadratic out-of-plane bend	150	75	mm	2.0E-14	7.0E-15
5	lateral shift	0.15	1	mm	**1.9E-12**	6.5E-15
6	In plane rotation	1	2	mm at tip	2.5E-13	7.4E-17
7	In plane quadratic bend	5	5	mm at tip	1.4E-13	4.8E-17
8	Symmetric sine wave 1 cycles	25	25	um	1.9E-13	1.8E-13
9	Symmetric sine wave 2 cycles	5	10	um	6.1E-14	2.4E-13
10	Symmetric sine wave 4 cycles	3	1	um	**3.1E-12**	4.7E-13
11	Symmetric sine wave 8 cycles	4	2	um	3.7E-14	1.3E-14
12	Symmetric sine wave 12 cycles	5	5	um	1.3E-14	1.9E-14
13	Symmetric sine wave 16 cycles	25	10	um	1.5E-13	3.4E-14
14	Syymmetric sine wave 20 cycles	25	10	um	9.2E-14	2.0E-14
15	Antisymmetric sine wave 4 cycles	10	2	um	3.9E-13	9.0E-19
16	In plane elliptical truss deform.	n/a	0.02	eccentricity	3.9E-13	1.8E-16

are functions of position in the image plane. The cross term accounts for the 'homodyne' effect of the background flux interfering with the spatially random terms. A similar expression was derived for speckle fields by Aime and Soummer[26] and was used in the TPF-C error budget.[2] This equation was applied to each optical band. Our M-C simulations validate this equation under the assumption that all the modes are uncorrelated. Figure 7 shows several examples of our M-C simulation.

We assumed that the individual petal perturbations were uncorrelated and normally distributed with the amplitude given in Table 4. We assumed that the global perturbations had amplitudes fixed at the values shown in Table 4, but had a random positive or negative sign. This allows us to specify an envelope for a global error, e.g. the magnitude of the mean radial position error for all petals must be less than 100 um (global perturbation 3).

Table 4 shows the perturbation amplitude for the individual and global terms, and the contribution that each makes (if taken on its own) to the r.m.s. and mean background. Numbers in **bold** are the most significant contributors. These are the terms that presently appear to be the most challenging to control in manufacturing or deployment. The r.m.s. and mean contrast in the last two columns are evaluated at the longest wavelength (0.55 um) which is generally the most sensitive to perturbations.

Table 5 shows the performance of the system. The r.m.s. contrast is better than 10^{-11} at all bands and the mean light level is well below the expected zodiacal + exozodiacal light level. When 1-m of cross-track error is included, the r.m.s. background level still meets the 10^{-11} requirement across the bandpass, but we have not included margin and we have not added in modes (e.g. petal edge step errors[9]) that might prove to be significant.

Table 5. Contrast in the image plane

wavelength (um)	0.25	0.3	0.35	0.4	0.45	0.5	0.55
rms	4.9E-12	7.8E-12	5.0E-12	5.3E-12	5.7E-12	8.4E-12	9.5E-12
mean	4.2E-12	5.2E-12	4.9E-12	5.7E-12	6.3E-12	9.8E-12	1.1E-11

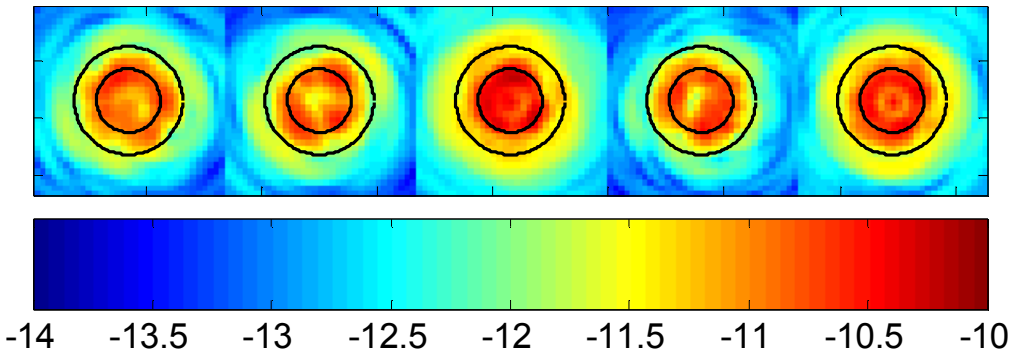

Figure 7. Five realizations of the image plane contrast for the allocated perturbations listed in Table 4. Single-petal errors were realizations of Gaussian deviates with standard deviation from the 3rd column of Table 4. Global errors realizations of fixed values (col. 4) with random sign. Circles indicate the IWA annulus centered at 90 mas. Images are the equally weighted composite across the bandpass 0.25-0.55 um.

7. CONCLUSION

We have achieved satisfying agreement on perturbation sensitivities, facilitated by being very specific about the perturbations to be analyzed. We have shown that independent models at NGAS and JPL are consistent to better than 5% in computing the main perturbation intensity in the telescope image plane and the change due to several perturbations. We find hypergaussian and optimized petal shapes yield very similar sensitivities when the same perturbations are applied. Using the JPL code, we have evaluated perturbation sensitivities of a strawman mission consisting of an optimized 34-m diameter starshade with 6.5-m long petals and a 2-m diameter telescope.

We have reached agreement on approaches to tolerance budgeting, beginning with the list of perturbations to be considered and the methods for exercising them. The major perturbations have been described in detail; the chosen set is representative of the errors that are most likely to affect performance. Some of our analysis used Monte Carlo methods to combine several perturbations at once, but most of our analysis so far has assumed that the perturbations are independent and static. Noecker[27] has described an approach to combining a basis set containing correlated and time-variable modes. We have laid the groundwork for implementing spreadsheet performance budgets based on sensitivities and statistically-based formulas for combining multiple errors.

We have presented an error budget that includes random perturbations on the petals and global perturbations common to all petals. The error budget meets the observational requirement of SNR > 4 with respect to the systematic noise floor for any operational spectral band. In this budget, some challenging requirements are identified, most notably global radial position, and mid-frequency sine waves on the petal edges.

We are still working to develop budget spreadsheets as a communicating/reporting tool and as a system engineering tool. We will continue to refine allocations and compare different designs by their tolerances. This will also facilitate a review and possible revision of technology readiness assessments, which will help inform technology roadmaps.

We have not yet studied the interaction of these perturbations with a starshade that is tilted (not perpendicular to the line of sight); this is a required operational mode in some designs that have limited solar viewing angles, especially a starshade for JWST.

We have considered but not yet developed other observational approaches that could greatly relax these requirements. For example, spinning the starshade on time scales equal to or shorter than the science observation would smear the speckles that are caused by manufacturing and deployment errors, resulting in annular scatter with little or no azimuthal component. This also tends to neutralize the dynamic terms that give rise to a systematic floor on planet sensitivity;

consequently we would be able to relax the static tolerances, perhaps by a large factor (3-10). Spinning does not solve all problems — it may not average out the thermal errors caused by solar heating and shadowing of the starshade support structures and spacecraft. But it will significantly relax the manufacturing and deployment tolerances associated with individual petals. This, along with the application of image processing algorithms to improve SNR, will be the subject of future work.

Acknowledgments

Part of this work was performed at the Jet Propulsion Laboratory, California Institute of Technology, under contract to the National Aeronautics and Space Administration. Government funding is acknowledged. We gratefully acknowledge Laurent Pueyo for helpful discussions and Doug Lisman for a critical reading of the manuscript and many helpful suggestions.

REFERENCES

[1] *Exoplanet Community Report*, Lawson, P. R., Traub, W. A., and Unwin, S. C., eds. JPL Publication 09-3 (2009).

[2] Shaklan, S. B., Marchen, L., Green, J. J., and Lay, O. P., "The Terrestrial Planet Finder Coronagraph Dynamics Error Budget," Proc. SPIE 5905, 59050D (2005).

[3] Lay, O. P., Martin, S. R., and Hunyadi, S. L, "Planet-finding performance of the TPF-I Emma architecture," Proc. SPIE 6693, 66930A (2007).

[4] Arenberg, J. W., Lo, A. S., Cash, W., and Polidan, R. S., "New Worlds Occulter performance: a first look," Proc. SPIE 6265, 62651W (2006).

[5] Shipley, A., Cash, W., Arenberg, J. W., Lo, A. S., "New Worlds Observer Tolerance Overview," Proc. SPIE 6687, 66871A-66871A-11 (2007).

[6] Arenberg, J. W., et al, "Sensitivity analysis of the New Worlds starshade's shadow," Proc. SPIE 7010, 70101V-70101V-11 (2008).

[7] Lyon, R., et al, "Externally occulted terrestrial planet finder coronagraph: simulations and sensitivities," Proc. SPIE 6687, 668719-12 (2007).

[8] Dumont, P., Shaklan, S., Cady E., Kasdin, J., Vanderbei, R., "Analysis of external occulters in the presence of defects," Proc. SPIE 7440, 744008-12 (2009).

[9] Glassman, T., et al., 2010, SPIE, 7731-188 (this conference).

[10] Kasdin, N. J., et al, "Occulter design for THEIA," Proc. SPIE 7440, 744005-8 (2009).

[11] Vanderbei, R. J., Cady, E., Kasdin, N. J., "Optimal Occulter Design for Finding Extrasolar Planets," ApJ, 665, 794-798 (2007).

[12] Glassman, T., et al. 2010 in preparation

[13] Cash, W. "Detection of Earth-like planets around nearby stars using a petal-shaped occulter," Nature, 442, 51-53 (2006).

[14] Dubra, A. and Ferrari, J. "Diffraction from an arbitrary aperture", Am. J. Phys., 67, 87-92 (1999).

[15] Schindhelm, E., et al, "Laboratory studies of petal-shaped occulters," Proc. SPIE 6693, 669305-1-8 (2007).

[16] Noecker, C., "List of perturbation functions to be used in external occulter tolerancing," Ball Aerospace Systems Engineering Report #2340406 (2010).

[17] Arenberg, J. W., Glassman, T., and Lo, A. S., "Effects of scattered light on the performance of the New Worlds Starshade," Proc. SPIE 6693, 66931E (2007).

[18] Lillie, C., Lo, A., Daily, D., Glassman, T., "New Worlds Observer precursor mission," Proc. of The Spirit of Lyot 2007 (Berkeley, 2007).

[19] Soummer, R., et al, "A starshade for JWST: science goals and optimization," Proc. SPIE 7440, 74400A (2009).

[20] Kasdin, N. J. et al. 2010, BAAS, 41, 287.

[21] Cady, E., Shaklan, S. B., Kasdin, J., Spergel, D., "A method for modifying occulter shapes," Proc. SPIE 7440, 744007-8 (2009).

[22] Thomson, M. and D. Lisman, "Occulting Ozone Observatory starshade design and development," Proc SPIE 7731-191 (this conference).

[23] Hunyadi, S., Shaklan, S. B., Brown, R. A., "The lighter side of TPF-C: evaluating the scientific gain from a smaller mission concept," Proc. SPIE 6693, 66930Q (2007).

[24] Savransky, D., Kasdin, N. J., and Cady, E., "Analyzing the Designs of Planet-Finding Missions," PASP 122, 401-419 (2010).
[25] Lafrenière, D., et al, "A new algorithm for point-spread function subtraction in high-contrast imaging: a demonstration with angular differential imaging," ApJ, 660, 770-780 (2007).
[26] Aime, C., and Soummer, R., "The usefulness and limits of coronagraphy in the presence of pinned speckles," ApJ 612, L85-L88 (2004).
[27] Noecker, C. "Arithmetic for budgeting errors of an external occulter for planet finding," Ball Aerospace Systems Engineering Report #2341590 (2010)

APPENDIX

We derive the variance of the scattered light, Eq. 4. We begin with

$$\sigma^2 = \langle I^2 \rangle - \langle I \rangle^2 - \sigma_b^2 \qquad \text{A1}$$

where I is the intensity of the scattered light and σ_b^2 is the variance of azimuthally-independent, radial-only background. The azimuthally-independent light does not impact our ability to sense the planet, thus we subtract the variations associated with it. Eq. A1 is then the variance of the light that is spatially variant on the scale of the telescope point spread function. We anticipate the use of standard filtering approaches such as matched filters that distinguish the planet light from background annulus light.

The intensity is given by $I = |E_b + E_r|^2$ where E_b is electric field of the background light containing only radial terms, and E_r is the electric field of the scatter containing terms with both random azimuthal and radial components. The background light arises from global perturbations (petal errors that have the same magnitude and sign on all petals) in addition to the nominal field. Strictly speaking, a fraction of the scatter in these terms has an azimuthal component periodic with the petal structure, but the azimuthal component is much smaller than the bias level. The random light comes from single-petal perturbations:

$$E_b = \sum_i E_{g,i} \quad \text{and} \quad E_r = \sum_j E_{s,j} \qquad \text{A2}$$

where $E_{g,i}$ is the electric field arising from the ith global perturbation and $E_{s,j}$ is the electric field arising from the jth single-petal perturbation. We assume all of these perturbations are uncorrelated, so that

$$\langle E_{g,i} E_{g,k\neq i} \rangle = 0, \quad \langle E_{s,j} E_{s,m\neq j} \rangle = 0, \quad \text{and } \langle E_{g,i} E_{s,j} \rangle = 0 \ . \qquad \text{A3}$$

We also assume the perturbations have zero mean, and are symmetrically distributed (*e.g.,* Gaussian or uniform distribution) so that the real and imaginary components of the scattered fields are equally likely and of equal amplitude:

$$\langle E_b^{R2} \rangle = \langle E_b^{I2} \rangle, \quad \langle E_r^{R2} \rangle = \langle E_r^{I2} \rangle, \quad \text{and} \quad \langle E_r^R E_r^I \rangle = 0 \qquad \text{A4}$$

where the *R* and *I* superscripts refer to the real and imaginary components of the field.

We are now ready to evaluate the terms in Eq. A1. The second moment of intensity is

$$\begin{aligned} \langle I^2 \rangle = \langle |E_b + E_r|^4 \rangle &= \langle |E_b|^4 \rangle + \langle |E_r|^4 \rangle + 2\langle |E_b|^2 \rangle \langle |E_r|^2 \rangle + 4\langle \left(\mathrm{Re}(E_b E_r^*)\right)^2 \rangle \\ &= \langle I_b^2 \rangle + \langle I_r^2 \rangle + 2\langle I_b \rangle \langle I_r \rangle + 4\langle \left(\mathrm{Re}(E_b E_r^*)\right)^2 \rangle \ . \end{aligned} \qquad \text{A5}$$

Evaluating the last term of Eq. A5, we have $\mathrm{Re}\langle E_b E_r^* \rangle = \mathrm{E_b^R E_r^R} + \mathrm{E_b^I E_r^I}$ and use Eq A4 to obtain

$$4\langle \left(\mathrm{Re}(E_b E_r^*)\right)^2 \rangle = 4\langle (E_b^R E_r^R)^2 + (E_b^I E_r^I)^2 \rangle = 8\langle E_b^{R2} \rangle \langle E_r^{R2} \rangle \quad . \qquad \text{A6}$$

We are not quite done simplifying this expression. We can take advantage of the symmetry and uncorrelated properties of the real and imaginary components to show that

$$\langle I_b\rangle\langle I_r\rangle = \langle|E_b|^2\rangle\langle|E_r|^2\rangle = \langle E_b^{R2} + E_b^{I2}\rangle\langle E_r^{R2} + E_r^{I2}\rangle = 4\langle E_b^{R2}\rangle\langle E_r^{R2}\rangle \quad . \tag{A7}$$

We can finally write rewrite eq. A5 as

$$\langle I^2\rangle = \langle I_b^2\rangle + \langle I_r^2\rangle + 4\langle I_b\rangle\langle I_r\rangle \quad . \tag{A8}$$

The second term in Eq. A1 is

$$\langle I\rangle^2 = \langle|E_b + E_r|^2\rangle^2 \quad . \tag{A9}$$

We invoke equation A3 and find

$$\langle I\rangle^2 = \langle|E_b|^2 + |E_r|^2\rangle^2 = \langle I_b + I_r\rangle^2 = \langle I_b\rangle^2 + \langle I_r\rangle^2 + 2\langle I_b\rangle\langle I_r\rangle \quad . \tag{A10}$$

Evaluating eqs. A7 and A10 in Eq. A1, we find

$$\sigma^2 = \langle {I_b}^2\rangle - \langle I_b\rangle^2 + \langle {I_r}^2\rangle - \langle I_r\rangle^2 + 2\langle I_b\rangle\langle I_r\rangle - \sigma_b^2 \tag{A11}$$

The first two terms are by definition the variance of the background scatter, $\sigma_b^2 = \langle {I_b}^2\rangle - \langle I_b\rangle^2$, and the next two terms are the variance of the random scatter $\sigma_r^2 = \langle {I_r}^2\rangle - \langle I_r\rangle^2$ so that we are left with

$$\sigma^2 = 2\langle I_b\rangle\langle I_r\rangle + \sigma_r^2 \tag{A12}$$

which is Eq. 4.

In practice, we use Monte-Carlo simulations to evaluate the mean contrast and contrast variance, perturbation by perturbation, for the chosen statistics (e.g. normal distribution for single-petal perturbations, bimodal for global perturbations), and we form tables of these terms in an Excel spreadsheet. The intensity scales as the square of the allocated perturbation amplitude, while the intensity variance scales as the 4th power of the amplitude. Terms are then summed and combined according to Eq. 4.